Machine Learning Accelerates the Discovery of Design Rules and Exceptions in Stable Metal–Oxo Intermediate Formation

ACS Catalysis

Research Article

Cite This: ACS Catal. 2019, 9, 8243−8255

pubs.acs.org/acscatalysis

Machine Learning Accelerates the Discovery of Design Rules and Exceptions in Stable Metal−Oxo Intermediate Formation

Aditya Nandy,[†,‡] Jiazhou Zhu,[§] Jon Paul Janet,[†] Chenru Duan,[†,‡] Rachel B. Getman,[*,§] and Heather J. Kulik[*,†]

[†]Department of Chemical Engineering and [‡]Department of Chemistry, Massachusetts Institute of Technology, Cambridge, Massachusetts 02139, United States

[§]Department of Chemical & Biomolecular Engineering, Clemson University, Clemson, South Carolina 29634, United States

Supporting Information

ABSTRACT: Metal−oxo moieties are important catalytic intermediates in the selective partial oxidation of hydrocarbons and in water splitting. Stable metal−oxo species have reactive properties that vary depending on the spin state of the metal, complicating the development of structure−property relationships. To overcome these challenges, we train machine-learning (ML) models capable of predicting metal−oxo formation energies across a range of first-row metals, oxidation states, and spin states. Using connectivity-only features tailored for inorganic chemistry as inputs to kernel ridge regression or artificial neural network (ANN) ML models, we achieve good mean absolute errors (4−5 kcal/mol) on set-aside test data across a range of ligand orientations. Analysis of feature importance for oxo formation energy prediction reveals the dominance of nonlocal, electronic ligand properties in contrast to other transition metal complex properties (e.g., spin-state or ionization potential). We enumerate the theoretical catalyst space with an ANN, revealing expected trends in oxo formation energetics, such as destabilization of the metal−oxo species with increasing d-filling, as well as exceptions, such as weak correlations with indicators of oxidative stability of the metal in the resting state or unexpected spin-state dependence in reactivity. We carry out uncertainty-aware evolutionary optimization using the ANN to explore a >37 000 candidate catalyst space. New metal and oxidation state combinations are uncovered and validated with density functional theory (DFT), including counterintuitive oxo formation energies for oxidatively stable complexes. This approach doubles the density of confirmed DFT leads in originally sparsely populated regions of property space, highlighting the potential of ML-model-driven discovery to uncover catalyst design rules and exceptions.

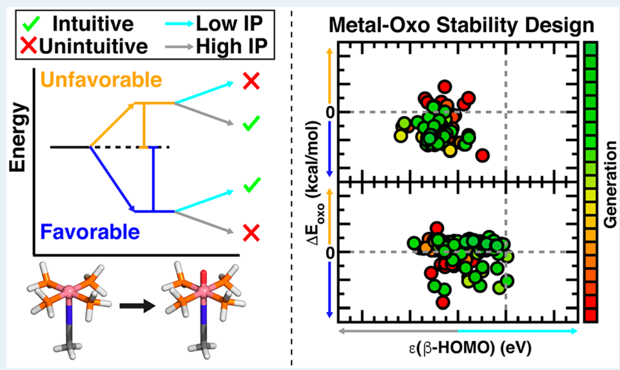

KEYWORDS: *metal−oxo species, machine learning, density functional theory, spin-state-dependent reactivity, transition metal catalysis, artificial neural networks*

1. INTRODUCTION

The selective partial oxidation of alkanes (e.g., methane to methanol[1,2]) represents one of the foremost challenges in catalysis. Despite intense focus,[3−8] the design of highly selective and active synthetic catalysts has been limited by overoxidation as a result of the higher reactivity of products than reactants. Conversely, it is known that enzymes readily catalyze selective partial oxidation through the formation of high-valent metal−oxo (e.g., Fe(IV)=O) species.[9−12] These biological catalysts have motivated the development of bioinspired molecular[13−17] and extended[18] (e.g., zeolite[19] or metal−organic framework[20]) catalysts for C−H activation.

High-valent[21] (e.g., Fe(IV),[22,23] Fe(V),[24,25] Mn(IV),[26] or Mn(V)[27,28]) metal−oxo species are believed to be central to selective partial oxidation, and the difficulty with which they are isolated and characterized spectroscopically[23,29−32] motivates computational screening[33,34] and characterization.[35−37] High-throughput computational catalyst screening can extend beyond the small number of complexes and materials that have been demonstrated experimentally to support formation of high-valent metal−oxo species, instead permitting the discovery of design rules across the periodic table.[38,39] Such an effort is motivated, for example, by the fact that both late (e.g., Co) and low-valent (e.g., Fe(III)−O) transition metals had been thought to be nearing the "oxo wall",[40−43] but an increasing number of Co(IV)=O complexes have been recently characterized.[44−46] The computational study of such open-shell species with variable oxidation state is made more

Received: May 24, 2019
Revised: June 29, 2019
Published: July 23, 2019

complex by the role of electron spin, an inherently quantum-mechanical property. Distinct metal–oxo spin states can have strongly differing reactivity,[32,47−52] with the highest rates expected for high-spin (i.e., quintet) Fe(IV)═O complexes that mimic enzymatic systems.[53] For each spin state and complex, stability can be as much of a challenge,[16,54−57] with some of the most reactive species deactivating significantly faster than less reactive species.

Large-scale computational screening[33,58−70] has the potential to uncover which chemical environments enable formation of stable metal–oxo species. Widely successful approaches in computational screening for heterogeneous catalysis, such as linear scaling relationships[65,68,71−77] or established quantum mechanical (QM) descriptors (e.g., the d-band center[78−80] or other frontier orbital properties[61,70,81]), are expected[82] to be limited in their capacity to describe spin-state-dependent metal–oxo formation. Indeed, even for a fixed spin state, small geometric distortions have been shown to cause large deviations in linear free energy relationships and alter the frontier orbital energies[67] relevant for metal–oxo formation. Noncovalent interactions relevant in single-site catalysts have also been shown to disrupt scaling relations.[72,73,76,77,83−87] A screen of multiple metal, spin, and oxidation states in combination with a wide range of ligands is motivated by the desire to reveal the extent to which conventional scaling rules apply or may be broken in selective partial oxidation, but the sheer combinatorial challenge of such a screen requires a different approach than standard first-principles screening.

Machine-learning (ML) property prediction models have the promise of accelerating discovery by enabling property prediction in seconds instead of the hours required by first-principles computational screening.[88−92] In recent years, ML has been increasingly applied to accelerate mechanism[93,94] or materials[95−97] discovery of closed-shell and/or bulk metal heterogeneous catalysts. Significant progress has also been made in the prediction of fundamentally quantum-mechanical properties of open-shell transition metal complexes, such as frontier orbital energies,[98,99] ionization or redox potentials,[92,100,101] and spin-state ordering.[102−104] Successful ML models have not yet been demonstrated in challenging open-shell, single-site catalysts that exhibit spin-state-dependent reactivity. It is in this area that nonlinear ML models may have the greatest promise to accelerate high-throughput screening due to the weak predictive capability of linear scaling relations, which are frequently distorted or broken in isolated, under-coordinated metal sites.[67,105,106]

In this work, we train ML models to predict spin-state-dependent metal–oxo formation energies in octahedral model catalysts. Using these models, we reveal unexpected structure–property trends in spin-state-dependent reactivity and the limits of the relationships between metal–oxo formation and a conventionally used QM descriptor (i.e., a frontier orbital energy). We then explore large (ca. 37 000) candidate catalyst spaces to discover wholly new complexes with unexpected combinations of oxidative stability and oxo formation energy.

2. CATALYSIS MODELS

To evaluate the difficulty of machine-learning tasks for open-shell transition metal catalysis, we focus on the reaction energy for the formation of high-valent oxo species essential in C–H activation.[21−28] We define this oxo formation energy, ΔE_{oxo}, as the difference in total electronic energy between a high-valent oxo species and its corresponding empty-site structure in the same spin state with respect to a triplet oxygen reference, where the empty-site metal's oxidation state is n = 2 or 3

$$\Delta E_{oxo} = E(\mathrm{M}(n{+}2){=}\mathrm{O}) - E(\mathrm{M}(n)\cdots) - \frac{1}{2}E(^{3}\mathrm{O}_2) \qquad (1)$$

Two data sets, the equatorially symmetric data set and the equatorially asymmetric data set, were designed to probe a wide range of effects on ΔE_{oxo} values in octahedral, open-shell transition metal complexes. In addition to the machine-learning models, these two data sets represent 1200 new catalyst energetic evaluations carried out solely for the present work.

The equatorially symmetric (ES) data set consists of 712 ΔE_{oxo} values for complexes with one equatorial and one distal axial ligand type (Figure 1). Total complex charge varies across

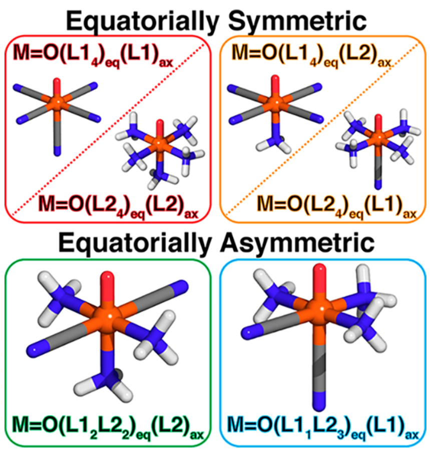

Figure 1. Representative structures for the equatorially symmetric (top) and equatorially asymmetric (bottom) data sets, which each have up to two unique ligand types, L1 and L2 (here L1 = CN^-, L2 = NH_3). The metal is shown as an orange sphere, and other atoms are shown as sticks, with oxygen in red, nitrogen in blue, and carbon in gray.

catalyst models with individual ligand charge but is preserved between the oxo (M(IV)═O or M(V)═O) and the empty-site (M(II) or M(III)) complexes (M = Cr, Mn, Fe, or Co, Figure 2). Complexes are comprised of up to two distinct ligands from a pool of 29 ligands: 9 negatively charged (e.g., acac, CN^-, Cl^-, and pyrrole) and 20 neutral (e.g., CO, NH_3, bipyridine, or furan) (Figure 2). This ligand pool was designed to broadly sample ligand fields and enable comparison to prior work.[67,102,103] All bidentate or tetradentate ligands can only serve as equatorial ligands.

For this data set, high-valent oxo and empty-site species were studied in their low-spin (LS), intermediate-spin (IS), and high-spin (HS) states, where defined, for both M(n+2) and M(n) oxidation states: doublet for d^1 Cr(V) and d^3 Cr(III), singlet/triplet for d^2 Cr(IV)/Mn(V) and d^4 Cr(II)/Mn(III), doublet/quartet for d^3 Mn(IV)/Fe(V) and d^5 Mn(II)/Fe(III), singlet/triplet/quintet for d^4 Fe(IV)/Co(V) and d^6 Fe(II)/Co(III), and doublet/quartet for d^5 Co(IV) and d^7 Co(II). The final data set is broadly balanced across each of these metals, oxidation states, and spin states (Supporting Information Figure S1).

The equatorially asymmetric (EA) data set consists of 488 ΔE_{oxo} values constructed from a smaller pool of 18 ligand types, 7 of which overlap with the ES data set (Figures 1 and 2

DOI: 10.1021/acscatal.9b02165
ACS Catal. 2019, 9, 8243−8255

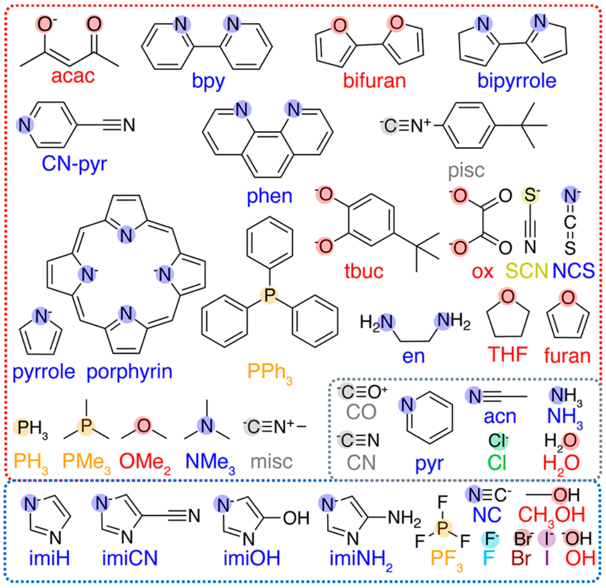

Figure 2. Ligands studied in this work: in the equatorially symmetric data set only (red rectangle), equatorially asymmetric data set only (blue rectangle), and in both sets (gray rectangle). Ligand atoms that coordinate the metal are shaded with translucent circles colored by element: red for oxygen, dark blue for nitrogen, orange for phosphorus, yellow for sulfur, gray for carbon, light blue for fluorine, dark red for bromine, and purple for iodine. Ligand charges are denoted on the figure.

and Supporting Information Table S1). Catalyst models consist of two ligand types in the following arrangements: (i) $M(IV){=}O(L1_2L2_2)_{eq}(L2)_{ax}$, where identical ligands lie trans with respect to each other in the equatorial (eq) plane, and (ii) $M(IV){=}O(L1_1L2_3)_{eq}(L1)_{ax}$, where the ligand in the distal axial position is identical to one of the four equatorial ligands (Figure 1). For either configuration, L1 is selected from 12 possible negatively charged ligands (e.g., imidazolides, Cl^-, CN^-) and L2 is selected from 6 neutral ligands (e.g., H_2O, CO, pyridine, see Figures 1 and 2). This data set size is smaller in part due to consideration of only the M(IV)=O species and smaller ligand pool, but it includes a wider range of first-row metals (i.e., M = Cr, Mn, Fe, Co, Ni, or Cu), including those past the so-called "oxo wall".[41−43]

For this data set, high-valent oxo and empty-site species were also studied in their LS, IS, and HS states with the additional relevant definitions: singlet/triplet for d^6 Ni(IV) and d^8 Ni(II) and doublet for d^7 Cu(IV) and d^9 Cu(II). The final data set is broadly balanced across each of these metal, oxidation state, and spin states (Supporting Information Figure S2).

3. METHODS

3.1. Simulation Details. *3.1.1. ES Data Set.* All gas-phase geometry optimizations and single-point energy calculations in the ES data set were performed using density functional theory (DFT) with TeraChem.[107,108] The B3LYP[109−111] global hybrid functional was employed with the empirical D3 dispersion correction[112] using Becke−Johnson[113−115] damping. The LANL2DZ[116] effective core potential was used for transition metals, and the 6-31G* basis set was employed for remaining atoms to enable rapid data set generation and comparison to prior inorganic chemistry machine-learning studies.[98,101−103] Except for singlet spin states, all simulations were carried out in an unrestricted formalism with level shifting (Supporting Information Text S1). All initial geometries were generated with molSimplify,[117] as automated with mAD[98] for up to five 24 h run-time job resubmissions. Geometry optimizations of the oxo species were carried out with geometry checks[98] prior to each resubmission, and single-point energies for the empty-site configuration were obtained only on the oxo structures that passed these checks (Supporting Information Text S1 and Table S2). From 1650 initial oxo/empty-site structure pairs, we excluded pairs if either structure did not satisfy specific criteria for geometry quality or $\langle S^2 \rangle$ values, as in prior work,[92,98,103] as well as metal spin density localized on the ligand instead of the metal, leading to a total data set size of 712 ΔE_{oxo} values (Supporting Information Table S3 and Figure S3).

3.1.2. EA Data Set. The EA data set was independently generated by some of the authors and therefore followed a distinct established protocol.[70,118] All gas-phase geometry optimizations and single-point energy calculations in the EA data set were performed using DFT in Gaussian09 Rev. B.01[119] with the M06-L[120] functional and def2-TZVP[121] basis set to enable comparison to prior studies. All spin states, including singlets, were treated with an unrestricted formalism. For this data set, constrained geometry optimizations with all other settings as default were performed on the empty-site structure to enforce 90° angles for all ligand−metal−ligand angles between adjacent ligands. Upon convergence of the empty-site structure, an oxygen atom was added to the structure in the axial position and only the metal−oxo bond was optimized with all other atoms frozen. This data set was verified by checking manually for proton transfer or ligand detachment.

3.2. Machine-Learning Models and Representations. The molecular representations used in this work are revised autocorrelations (RACs),[101] which have been demonstrated for prediction of spin-splitting energetics,[101] redox or ionization potentials,[100,101] frontier orbital energies,[98] and bond lengths.[101] RACs are extended[101] autocorrelations[122] tailored for transition metal chemistry that are products and differences on the molecular graph. In practice, around 150 RAC descriptors make up the complete feature set prior to feature selection (see details in Supporting Information Text S2).

Two types of ML models are trained in this work: (i) kernel ridge regression (KRR) models are used for feature selection and analysis, and (ii) artificial neural network (ANN) models are used for catalyst space exploration. The KRR models were trained on full RACs[101] and feature-selected subsets obtained with random forest-ranked recursive feature addition (RF-RFA) following an established protocol[98] (Supporting Information Text S1 and Figure S4). KRR training used scikit-learn[123] with grid search to obtain regularization, α, and inverse kernel width, γ, hyperparameters (Supporting Information Table S4). ANN models were trained on the full RACs in Keras[124] with TensorFlow[125] as the backend (Supporting Information Figures S5−S8 and Tables S5 and S6). Hyperparameters and ANN architectures were optimized using the HyperOpt[126] Python library with the Adam optimizer[127] and dropout regularization. For all models, we used an 80/20 train/test partition, and the ranges of the training data were used to normalize all inputs and outputs. Decision tree analysis in scikit-learn[123] used a maximum split

DOI: 10.1021/acscatal.9b02165
ACS Catal. 2019, 9, 8243−8255

of five and a maximum tree depth of two, which were selected to reveal dominant trends.

4. RESULTS AND DISCUSSION

4.1. Data Sets and Model Performance. The range of ΔE_{oxo} values observed in the 712 equatorially symmetric and 488 equatorially asymmetric data set complexes is comparable, from as low as −105 kcal/mol to as high as 75 kcal/mol (Supporting Information Figure S9). Across both data sets Cr and Mn complexes in all spin states have the most exothermic ΔE_{oxo} values, midrow Fe or Co complexes are more variable, and ΔE_{oxo} is exclusively endothermic for the later Ni and Cu transition metals. Although the metal is a strong determinant in ΔE_{oxo} favorability, the large variation within each metal motivates the training of ML models and further evaluation of chemical trends.

We start by extending our prior approach of employing RAC features with KRR models in the prediction of octahedral spin-splitting energetics,[101] redox or ionization potential,[92,101] metal−ligand bond length,[101] and frontier orbital energetics.[98] Assessing the degree to which this RAC/KRR approach is also predictive for ΔE_{oxo} will (i) identify if additional complexities arise for the learning task of spin-state-dependent catalyst energetics and (ii) determine if catalytic structure−property relationships differ from those obtained previously for other properties. Thus, we repeat our approach and make comparisons throughout to both model performance and observations from prior work.[92,98,101] The range of reaction energies in our ML model training data is comparable to those we studied[103] in ML models for spin-splitting energy (from −55 to 90 kcal/mol, Supporting Information Figure S10).

Feature selection from the full RAC feature set (ca. 150 descriptors) improves KRR model prediction errors[98,101] and provides insight into the most important descriptors for property prediction. Indeed, train/test mean absolute errors (MAEs) with the full set of RACs (7.5 and 9.5 kcal/mol) for the ES data set are reduced after RF-RFA feature selection (see section 3). A model trained on only the 22 features selected with RF-RFA has significantly lower train and test MAEs (2.2 and 5.5 kcal/mol), consistent with prior work[98] (Figure 3 and Supporting Information Figure S11 and Table S7). The full RAC/KRR performance is slightly better for the smaller EA data set (MAEs, train 2.3 and test 6.5 kcal/mol), but it is similarly improved after feature selection to 14 features (MAEs, train 1.5 and test 4.3 kcal/mol, Figure 3 and Supporting Information Figure S11, Table S8, and Text S3).

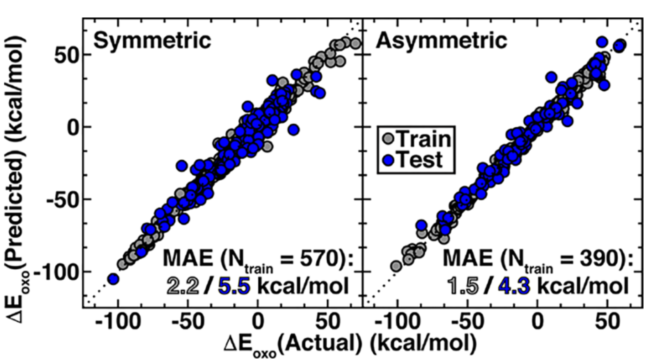

Figure 3. KRR model ΔE_{oxo} predictions compared to the DFT-calculated values for the equatorially symmetric (left) and equatorially asymmetric (right) data sets with RACs obtained from feature selection on each set, respectively. Number of training points used after the 80/20 train/test split is indicated in the inset along with the train (gray circles) and test (blue circles) mean absolute error (MAE) in kcal/mol. A black dotted parity line is also shown.

Decomposing errors by metal, oxidation state, and ligand identity provides insight into whether the RF-RFA/KRR model generalizes more poorly to specific metal−oxo complexes (Supporting Information Figures S12 and S13). The ES errors are lower for M(IV)═O complexes and higher for M(V)═O complexes absent from the EA data set (Supporting Information Figures S12 and S13). Nearly all of the high (>10 kcal/mol, ca. 30 cases) train or test set errors in the ES data set are indeed M(V)═O complexes with strong-field distal axial ligands (e.g., NMe_3, CO, pisc) or negatively charged (e.g., Cl^-, CN^-, acac, pyrrole) equatorial ligands. Across both data sets, test errors are generally lower for Mn and Fe in comparison to earlier or later metals (Supporting Information Figures S12 and S13). Comparison of errors across the EA data set ligand arrangements indicates slightly higher errors for the more asymmetric $M{=}O(L1_1L2_3)_{eq}(L1)_{ax}$ configuration, likely due to its lower abundance in the data set (37%, Supporting Information Figures S13 and S14).

Over both the ES and EA data sets, test MAEs of 4.3 and 5.8 kcal/mol are somewhat larger than the smallest we observed for spin-splitting energies[101,103] (ca. 1−3 kcal/mol) but roughly comparable to the 4 kcal/mol MAEs we observed for gas-phase ionization potential,[101] redox potential predictions,[101] or frontier orbital energies.[98] Given the wide diversity of ligand charges, structures, and metals as well as the fact that up to three ΔE_{oxo} values are predicted for each complex, the performance of the present KRR models is unexpectedly good. Spin-state-dependent reaction energetics of metal−oxo formation do not appear to be more challenging to predict than other properties of transition metal complexes.

4.2. Features that Influence Oxo Formation Energies. Beyond test set performance, comparison of RFA-selected features (oxo-22 for ES, oxo-14 for EA) reveals the length scale and character of molecular features that drive ΔE_{oxo} values (Figure 4, Supporting Information Tables S7 and S8). As in previous work,[101] the five heuristic atomic properties we correlate in approximately 150 RACs are (i) I, the identity, (ii) T, topology (i.e., connectivity), (iii) χ, Pauling electronegativity, (iv) S, the covalent radius, and (v) Z, the nuclear charge. These quantities are derived from products and differences of atomic properties on the molecular graph that we obtain either over the whole molecule (i.e., global features) or by counting bond paths outward from the metal center (e.g., first, second, or third coordination-sphere RACs, see Supporting Information Text S2). We compare the oxo-selected sets to a 26 RAC feature set (URAC-26) that was selected on spin-splitting data but has been shown to have the best balanced performance on ionization potential, redox potential, and bond length property prediction[92,101] (Figure 4). As could be expected from our preliminary analysis of the ΔE_{oxo} data set, properties of the metal, oxidation state, and spin are essential (ca. 20−25% of all features) and of comparable weight to those in URAC-26 (Figure 4, Supporting Information Table S9).

We previously found metal-coordinating atoms in the first coordination sphere to be important in URAC-26 and related metal-local feature sets for prediction of spin splitting,[103] an observation that holds for the ES oxo-22 feature set but not for the EA oxo-14 feature set (Figure 4). Differences in feature

DOI: 10.1021/acscatal.9b02165
ACS Catal. 2019, 9, 8243−8255

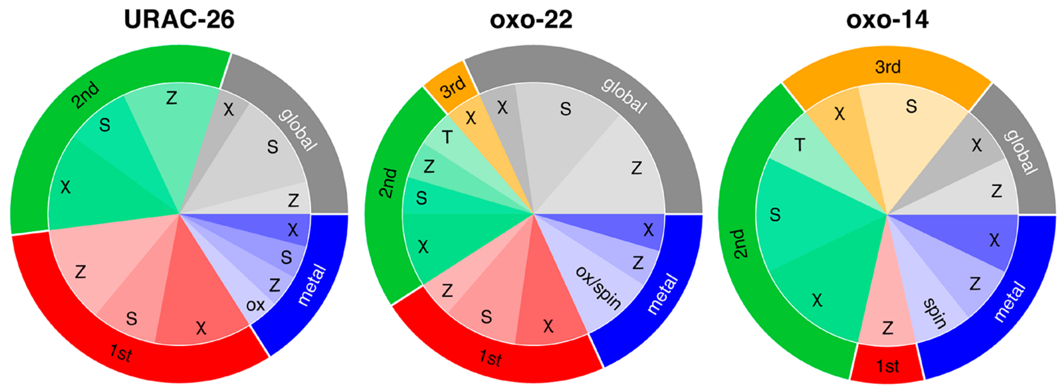

Figure 4. Pie charts of the URAC (26 features, left) features selected in prior work[92,101] compared to features selected by RF-RFA for oxo formation on the equatorially symmetric data set (22 features, middle) or the equatorially asymmetric data set (14 features, right). Features are grouped by the most distant atoms present: metal in blue, first coordination sphere in red, second coordination sphere in green, third coordination sphere in orange, or global features in gray. Within each distance category, the property (i.e., χ, S, T, or Z) is also indicated, and oxidation state (ox) and spin are assigned as metal-local properties.

selection over the ES and EA data sets can be attributed to the reduced size and variation of chemical composition for the EA data set (Supporting Information Text S4, Figures S15−S18, and Tables S10 and S11). Overall, feature analysis is broadly useful for interpreting data sets and ML models, but transferability of feature sets across different KRR prediction models is generally observed (Supporting Information Tables S9 and S12 and Figure S19).

The ΔE_{oxo}-selected features distinguish themselves from URAC-26 in their increased weight (ca. 35% vs 20%) of third coordination sphere or global features (Figure 4). Across the ES and EA data sets, these differences appear to be most critical to encoding through-bond ligand variations, as none of these metal-distant atoms are sufficiently proximal to form noncovalent interactions with the M(IV/V)=O species.[67,85−87] This feature analysis reveals oxo formation design rules: ΔE_{oxo} is affected not just by metal identity but also relatively metal-distant, through-bond electronic[101] (i.e., χ or Z) ligand functionalization, expanding upon previous experimental observations.[128]

4.3. Relation to QM Descriptors for Oxo Formation.

To accelerate and simplify computational screening, the β-HOMO level of Fe(II) complexes has been used as an estimate of the favorability of quintet Fe(IV)=O complex formation as long as this level has significant d character.[70] If this approximation holds[70] it provides an intuitive rationale that the metal must be easily oxidized for the high-valent species to form. Across the ES data set, most β-HOMO levels of Fe(II) complexes indeed have significant d character, with a few exceptions for conjugated ligands (e.g., pisc, bifuran, and cyanopyridine), but this observation holds less well across metals (Supporting Information Figures S20 and S21 and Table S13). A large range of β-HOMO level values is observed from around −30 to +8 eV, where the unphysically positive β-HOMO levels correspond to cases where high negative complex charge leads to poorly bound electrons at the hybrid DFT level of theory (Supporting Information Figure S22).[129,130] Over the full ES data set, ΔE_{oxo} and the β-HOMO level correlate only weakly overall and within a single metal, regardless of d character in the orbital (Figure 5).

As an example of the ease with which this β-HOMO/ΔE_{oxo} design rule may be broken, $S = 0$ Co(V)=O$(CO)_4(NH_3)$ and Mn(V)=O$(CO)_5$ have comparably deep β-HOMO levels (from ca. −26 to −27 eV), but ΔE_{oxo} is unfavorable by the

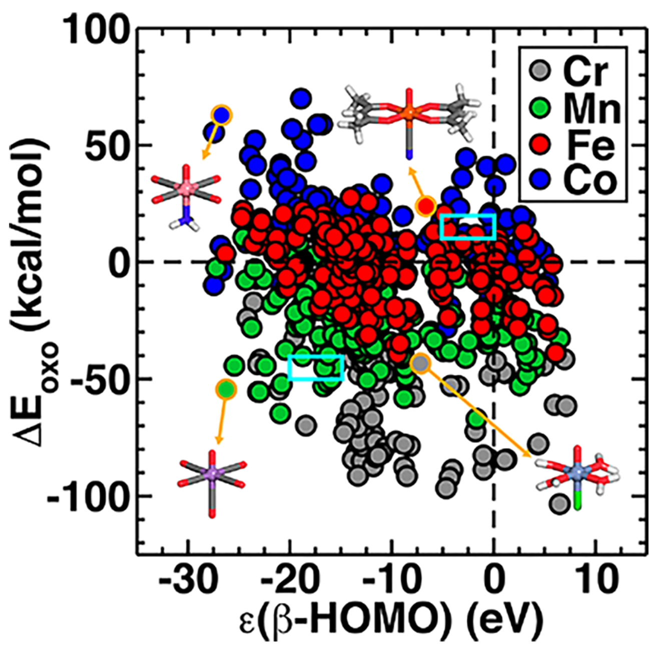

Figure 5. Empty-site structure β-HOMO level (in eV) vs ΔE_{oxo} (in kcal/mol) for the 712 structures in the equatorially symmetric set, colored by metal identity. Four representative structures are shown as insets: (top left) $S = 0$ Co(V)=O$(CO)_4(NH_3)$, (top right) $S = 1/2$ Fe(V)=O$(acac)_2(CN^-)$, (bottom left) $S = 0$ Mn(V)=O$(CO)_5$, (bottom right) $S = 1$ Cr(IV)=O$(H_2O)_4(Cl^-)$. Atoms are colored as follows: purple for Mn, pink for Co, light blue for Cr, red for O, blue for N, white for H, gray for C, and green for Cl. Cyan rectangles for Zone 1 (bottom, left) and Zone 2 (top, right) are also shown.

same magnitude for Co(V)=O (55.4 kcal/mol) as it is favorable for Mn(V)=O (−54.4 kcal/mol, Figure 5). Weaker field ligands (e.g., $S = 1/2$ Fe(V)=O$(acac)_2(CN^-)$ and $S = 1$ Cr(IV)=O$(H_2O)_4(Cl^-)$) correspond to shallower β-HOMO levels (e.g., from −7 to −9 eV), but ΔE_{oxo} values span a large range of endothermic and exothermic values for these complexes (Fe(V)=O 23.9 kcal/mol, Cr(IV)=O 46.5 kcal/mol, Figure 5). Even within a fixed metal, variations of tens of electronvolts of the β-HOMO level can be observed at fixed ΔE_{oxo} values or 50−100 kcal/mol variations of ΔE_{oxo} at fixed β-HOMO level; these observations suggest the possibility of orthogonally tuning frontier orbital energies (e.g., for resting

DOI: 10.1021/acscatal.9b02165
ACS Catal. 2019, 9, 8243−8255

state complex oxidative stability) and oxo formation energies (e.g., for reactivity).

Given the weak correlation between the β-HOMO level and ΔE_{oxo}, we developed a separate ML model to predict the β-HOMO level. We trained RF-RFA KRR models on the ES data set to obtain a test MAE of 0.44 eV that was somewhat higher than our prior frontier orbital energy models[98] (Supporting Information Figures S23–S26). Analyzing the 33 selected features for the RF-RFA β-HOMO level KRR model reveals the physical basis for the weak correlation between the properties (Figure 4 and Supporting Information Figure S27 and Table S14). The 33 features selected for β-HOMO level prediction are predominantly global (76%) and third coordination sphere (21%) properties that now include an enhanced dependence on the coordination of atoms in the structure (i.e., T or I RACs), with only weak contributions from the metal or second coordination sphere (χ only) and none from the first coordination sphere. Given the strong role of complex size and ligand character in determining the β-HOMO level, ligand chemistry or metal identity would need to be fixed to establish a correlation to oxo formation energies.

4.4. Enumeration of a Theoretical Catalyst Space.

From the 29 ligands originally considered in the ES data set, there is a theoretical space of 9860 transition metal complexes formed from all allowed combinations of metals, oxidation and spin states, and ligands. Although this space is inherently interpolative in nature, only 7.2% (712 points: 570 in train, 142 in test) of this compound space was used during model construction. Failed calculations account for 9.5% (938 points) of the space, but the remaining 83.3% (8210 points) are complexes for which no DFT calculation had been attempted. We switch from KRR to ANN models for the full space enumeration due to our experience[103] that ANNs generalize better than KRR models at the cost of being harder to interpret (Supporting Information Figures S28–S34).

The ΔE_{oxo} and β-HOMO level value ranges across the ML-model-enumerated theoretical space suggest wide coverage of the full range of β-HOMO level values within a single metal and significant overlap across metals for ΔE_{oxo} values (Supporting Information Figure S35). To confirm these observations, we obtained DFT validation results on a set of 277 previously unseen complexes obtained from ML model minimum, median, or maximum ΔE_{oxo} values for each metal (Supporting Information Figures S31, S32, and S35 and Table S15). These new DFT results further reinforce the observation that ΔE_{oxo} values and the β-HOMO level can be tuned independently. As an example of this design exception, a 14 eV variation in β-HOMO level is observed with limited change in ΔE_{oxo} for two Co(V)=O complexes: Co(V)=O$(acac)_2(Cl^-)$ (β-HOMO = −6.2 eV, ΔE_{oxo} = 47.3 kcal/mol) vs Co(V)=O$(NH_3)_4(OMe_2)$ (β-HOMO = −20.6 eV, ΔE_{oxo} = 43.0 kcal/mol) (Figure 5 and Supporting Information Figure S36).

Because the points selected for validation were ΔE_{oxo} extrema in the ML-model-interpolated space, many such points exceed the bounds of the original 712 DFT points in the ES data set and are extrapolative in property space. For example, singlet Mn(V)=O complexes with equatorial phosphine ligands and weak-field (e.g., H_2O −73 kcal/mol or misc −68 kcal/mol) axial ligands have even more favorable ΔE_{oxo} values than had been observed (singlet Mn(V)=O$(pyrrole)_4(H_2O)$ −67 kcal/mol) before (Figure 6). Although most Fe(IV)=O complexes have favorable ΔE_{oxo} values, three new singlet Fe(IV)=O$(CO)_4$(ax) complexes (e.g., ax = pyridine 37 kcal/mol) exceed the original ES data set's highest ΔE_{oxo} value compound (Fe(IV)=O$(misc)_5$ 28 kcal/mol), reinforcing equatorial CO as unfavorable for oxo formation across a range of axial ligands (Figure 6). The quintet Co(V)=O$(CN^-)_4(H_2O)$ with the most favorable ΔE_{oxo} value (−28 kcal/mol) in the ES data set has also been exceeded by as much as 13 kcal/mol in the likely ground state singlet Co(V)=O$(PH_3)_4(CH_3CN)$ (−41 kcal/mol, Figure 6). Analysis of simultaneously deep β-HOMO levels (<−15 eV) and favorable ΔE_{oxo} values (<−50 kcal/mol) in the new DFT data set reveals that in addition to singlet Mn(V)=O complexes with N-coordinating ligands that we observed in the original ES data set, we now confirm that equatorial PH_3 and weak-field axial ligands (i.e., singlet Mn(V)=O$(PH_3)_4$(ax) where ax = misc, Cl^-, furan, or water) populate this zone (Supporting Information Table S16).

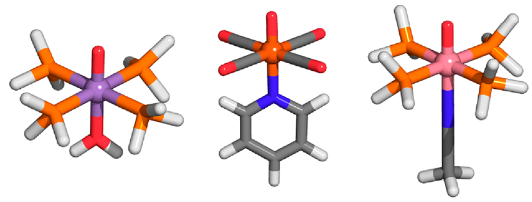

Figure 6. Three extreme points from the new data set with their ΔE_{oxo} values: singlet Mn(V)=O$(PH_3)_4(H_2O)$ (left), singlet Fe(IV)$(CO)_4$(pyridine) (middle), and singlet Co(V)=O$(PH_3)_4(CH_3CN)$ (right). Atoms in the stick structures of each lead compound are as follows: purple for Mn, dark orange for Fe, pink for Co, blue for N, gray for C, red for O, white for H, and orange for P.

Across the ANN-enumerated space, the ranges of metal-dependent ΔE_{oxo} values agree with the observation[131] that increasing d-electron count makes ΔE_{oxo} increasingly unfavorable as M–O π^* antibonding orbitals[132,133] become occupied (e.g., Fe or Co in Figure 7). The oxo formation energies for Cr and Mn complexes remain exothermic with an exceedingly small fraction (2.8%, 33 of 1160) of strong-field (e.g., CO) Mn(V) endothermic complexes.

Although spin-state dependence is expected[85] in Fe(IV)=O and its isoelectronic analogue, Co(V)=O, with more favorable ΔE_{oxo} values for HS and IS than LS, the enumerated data set reveals deeper chemical trends (Figure 7). The Fe(IV)=O complexes have the highest spin-state dependence when CO or CN^- are equatorial ligands, as is expected (favorable HS, IS; unfavorable LS, Supporting Information Figure S37). Weakening the equatorial or axial ligand (e.g., to H_2O or Cl^-) lessens this spin-state-dependent effect (Supporting Information Figures S37 and S38). Little spin-state dependence is evident in the Fe(V)=O complexes, which generally have similar LS and HS ΔE_{oxo} values (Supporting Information Figure S39). Starting from a weak equatorial ligand (e.g., water) in Fe(IV)=O without any apparent spin-state dependence and introducing strong-field ligands recovers moderate spin-state dependence on ΔE_{oxo} with favorable IS but unfavorable LS or HS values (Supporting Information Figures S37 and S38). Although isoelectronic Co(V)=O shows variation in the magnitudes of LS, IS, and HS ΔE_{oxo} values, nearly all are unfavorable (Supporting Information Figure S40). Interestingly, the combination of strong-field equatorial CO ligands with a weak-field (e.g., water) axial ligand that was observed to lessen Fe(IV)=O spin-state

DOI: 10.1021/acscatal.9b02165
ACS Catal. 2019, 9, 8243–8255

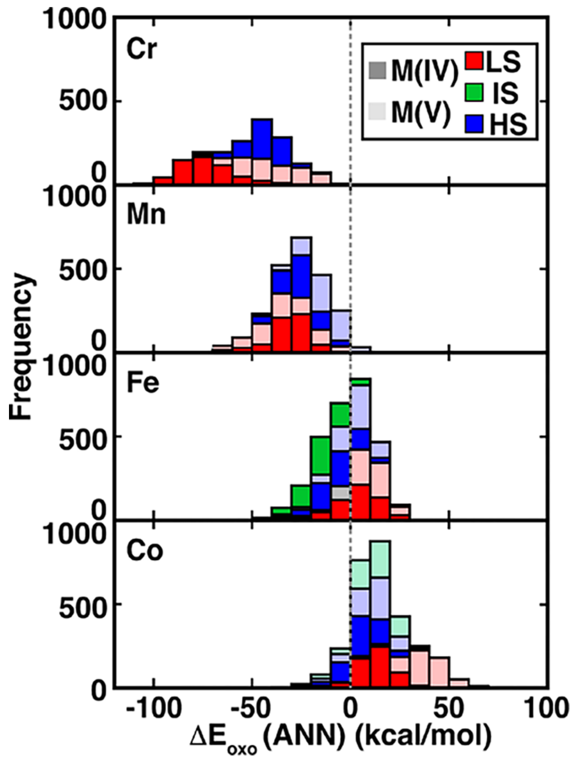

Figure 7. Distribution of oxo formation energies (in kcal/mol, bin size 10 kcal/mol) as predicted by the ANN for the 9860 equatorially symmetric complex space. Unnormalized counts are shown on the *y* axis, and histogram is colored by spin (red for low spin, LS, green for intermediate spin, IS, and blue for high spin, HS). The stacked histogram is shaded by oxidation state, with oxidation state +5 complexes represented by translucent coloring and oxidation state +4 complexes represented by opaque coloring.

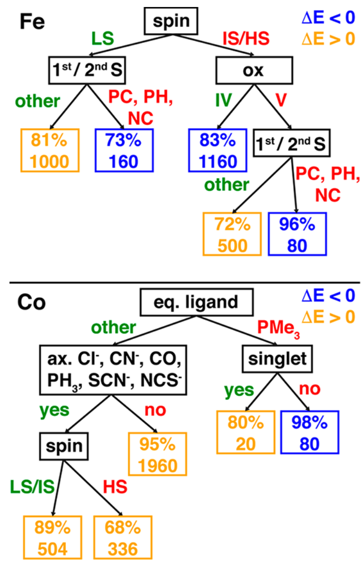

Figure 8. Decision tree analysis for essential descriptors of favorability for Fe (top) and Co (bottom) ANN-predicted ΔE_{oxo} binary decision tree divided by favorable ($\Delta E < 0$, blue) and unfavorable ($\Delta E > 0$, orange) for up to three levels total. Each leaf shows the percent of data corresponding to the case and total number of interpolated-space ANN values that correspond to each leaf.

dependence is instead predicted to strengthen Co(V)=O complex spin-state dependence (Supporting Information Figures S37 and S40).

To broadly uncover the governing factors in ΔE_{oxo} values, we carried out decision tree analysis on all enumerated Fe and Co ES-compatible complexes. Indeed, spin state is the largest driver for favorability, with most IS or HS complexes having favorable ΔE_{oxo} values (Figure 8). For the less stable high-spin Fe(V) complexes, strong-field ligand atoms in the equatorial plane first and second coordination spheres (e.g., P−C, P−H, and N−C first/second S) result in favorable ΔE_{oxo} values in the majority of cases (96%, Figure 8). Although such strong-field ligands are likely to bias toward LS ground states, this composition of the metal environment also is correlated with favorable ΔE_{oxo} values for both Fe(IV)=O and Fe(V)=O low-spin complexes (73%, Figure 8).

For Co, trends are less clear, likely because so few Co(IV/V)=O complexes are stable (Figures 7 and 8). From the decision tree analysis, IS and HS PMe_3 Co−oxo complexes are likely to have favorable ΔE_{oxo} values, but these are unlikely to be ground states (Figure 8). Indeed, from all interpolated complexes, only 11.8% (342 of 2900) are predicted by the ANN to have favorable ΔE_{oxo} values, and most have high- or intermediate-spin Co complexed with equatorial pnictogen atoms (108 N and 127 P) and axial strong-field coordinating atoms (129 C, 98 N, and 43 P). Although ligand field arguments suggest that HS or IS Co complexes would be rare, observations from our enumeration are consistent with the recent isolation and spectroscopic characterization of a metastable, N-coordinating complex, quartet $[(13\text{-TMC})Co(IV){=}O]^{2+}$ (13-TMC is 1,4,7,10-tetramethyl-1,4,7,10-tetraazacyclotridecane).[134]

4.5. ML-Driven Catalyst Space Exploration.

Inspired by the possibility of orthogonal empty-site β-HOMO level and ΔE_{oxo} tuning, we set out to search a larger design space of transition metal complexes. Our aim was to populate zones of empty-site β-HOMO level and ΔE_{oxo} that were under-populated in our original screen and that generally defy chemical intuition. For example, equatorially symmetric model catalysts could defy expectations by having (i) shallow empty-site β-HOMO levels, i.e., low ionization potentials, in combination with unfavorable ΔE_{oxo}, or (ii) deep empty-site β-HOMO levels, i.e., high ionization potentials, and favorable ΔE_{oxo}. In either case, we expect ANN-accelerated screening to reveal what catalyst model chemistries are most suited to breaking the relationship between resting state ionization potential and oxo formation favorability.

To carry out exploration beyond interpolative enumeration, we expanded the possible design space to a total of 56 different ligands (39 monodentate, 17 multidentate) in ES-compatible combinations, i.e., 27 more than the 29 originally included in the ES data set (Supporting Information Figure S41 and Table S17). Although several ligands were previously in the EA data set, we incorporated common ligands (e.g., tetraphenylporphyrin, phthalocyanine, bipyrimidine) and functionalizations of ES ligands (e.g., phendione, phenacac, mebpy). These new ligands enlarge the design space to 37 128 complexes (Supporting Information Table S18).

To accelerate discovery we combined our independent ANNs with a genetic algorithm (GA) optimization that we previously demonstrated for designing transition metal complexes with near-degenerate spin-splitting energies[102] and targeted band gaps.[98] For the present GA to optimize β-HOMO levels and ΔE_{oxo} simultaneously, we employed a composite fitness function with distance awareness to avoid

DOI: 10.1021/acscatal.9b02165
ACS Catal. 2019, 9, 8243−8255

points where the ANN will lack predictive power (Supporting Information Text S1, Figure S42, and Table S19). We then targeted two distinct regions of property space. For the first targeted zone (Zone 1), we selected ΔE_{oxo} between −40 and −50 kcal/mol along with a simultaneous empty-site β-HOMO level between −20 and −15 eV. Five ES complexes (train 5, test 0) are within this range, all of which are singlet Mn(V)═O coordinated in the equatorial plane by nitrogen atoms (e.g., ammonia or bpy see Figure 5). For the second targeted zone (Zone 2), we selected ΔE_{oxo} between 10 and 20 kcal/mol along with a simultaneous empty-site β-HOMO level between −5 and 0 eV. Six ES data points (train 5, test 1), two Fe(IV)═O and four isoelectronic Co(V)═O complexes, with negatively charged equatorial ligands reside in this zone. A GA approach is expected to help enrich both zones, where Zone 1 corresponds to a likely desired, stable catalyst, whereas Zone 2 corresponds to catalysts with less favorable energetics than would be predicted by the β-HOMO descriptor.

The composite-objective distance-controlled GA was run 10 times each for Zones 1 and 2 (Supporting Information Figures S43 and S44). For each zone, 50 leads (out of 137 total leads) generated from the runs were selected for further study with DFT. The majority of such structures correspond to unstable molecules at the DFT level, explaining why they were sparsely populated in our original DFT data set: only approximately 25% of the data (Zone 1: 13 leads, Zone 2: 15 leads) passed our standard electronic or geometric structure[135] checks (Supporting Information Table S20).

For Zone 1, i.e., favorable ΔE_{oxo} and high ionization potential, four new DFT lead compounds fully satisfy both criteria, nearly doubling the data we had in this range of properties, and the remaining complexes all satisfy the β-HOMO level range but fall narrowly below or above the target ΔE_{oxo} (Supporting Information Table S20). All four leads that fully satisfy the Zone 1 criteria are again singlet Mn(V)═O model catalysts, and three have the equatorial 2,2′-bypyrimidine ligand (bpym) that we introduced in the extended GA design space with a range of intermediate-field axial ligands (e.g., with a new imidazoline axial ligand, Figure 9 and Supporting Information Figure S41 and Table S17). Thus, DFT-validated lead compounds from the GA maintain and strengthen the observation that N-coordinated singlet Mn(V)═O model catalysts will have favorable ΔE_{oxo} and deep β-HOMO levels. Although the remaining 9 leads fall outside the Zone 1 target for ΔE_{oxo}, five cases are doublet Cr(V)═O complexes that still satisfy the deep β-HOMO level target (Supporting Information Table S20). The doublet Cr(V)═O(CN-pyr)$_4$(misc) is nearest to Zone 1 (DFT ΔE_{oxo} = −32 kcal/mol, β-HOMO = −16.5 eV), but the ANN predictions are eroded here due to the limited number of similar compounds in the training data. Overall, these DFT leads enhance data density in and around Zone 1. These complexes could be the focus of future computational study in selective partial oxidation (e.g., to understand the potential effect of deep β-HOMO levels).

For Zone 2, i.e., the unexpected combination of unfavorable ΔE_{oxo} and shallow β-HOMO level, two leads fall fully within both ranges after DFT validation and an additional four satisfy one of the two criteria. The two Zone 2 leads are quintet Fe(IV)═O or quartet Co(IV)═O porphyrin complexes with axial functionalized-isocyanide ligands (Figure 9). No prior training data in this zone had been Co(IV)═O, emphasizing the ability of this approach to discover new chemistry. All four leads that satisfy one of the two Zone 2 ranges are also

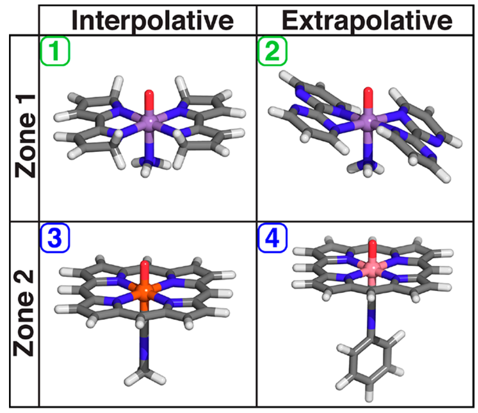

	ε(β-HOMO) (eV)		ΔE_{oxo} (kcal/mol)	
	DFT	ANN	DFT	ANN
1	-17.0	-15.7	-45.0	-47.7
2	-17.0	-15.9	-45.2	-41.3
3	-4.6	-4.1	20.0	10.2
4	-4.7	-4.2	11.3	10.2

Figure 9. Leads from the GA exploration, as predicted by the ANN and validated by DFT, that are observed for the two targeted zones 1 and 2 as described in the main text. Leads using ligands from the original equatorially symmetric ligand pool are labeled as "interpolative", and leads using ligands from a distinct, expanded ligand pool are labeled as "extrapolative". Atoms in the stick structures of each lead compound are as follows: purple for Mn, orange for Fe, pink for Co, blue for N, gray for C, red for O, and white for H.

Co(IV)═O complexes, e.g., (i) quartet complexes with equatorial acac ligands that have slightly more favorable DFT ΔE_{oxo} values (1−4 kcal/mol) than predicted by the ANN and (ii) a quartet complex with neutral furan equatorial ligands in combination with an expanded design space phosphorine axial ligand that has a weakly positive β-HOMO (1 eV, Supporting Information Table S20). For the remaining cases that failed to meet both Zone 2 criteria, most have weakly more favorable ΔE_{oxo} values combined with less favorable (i.e., positive) β-HOMO levels. These complexes represent cases where design based on β-HOMO level would fail and could therefore be used in future study to understand the limitations of QM descriptors for reactions involving oxo intermediates.

5. CONCLUSIONS

We trained ML models capable of predicting oxo formation reaction energies across a range of first-row metals, oxidation states, and spin states. With feature-selected ML models, we achieved set-aside test mean absolute errors of 4−5 kcal/mol across a range of ligand orientations. These comparable errors to other properties of open-shell transition metal complexes (e.g., ionization potential) suggest that spin-state-dependent catalyst structure−property relationships are no more challenging a learning task. Using feature selection, we observed that the most important features for predicting oxo formation energies were more nonlocal in nature than for spin-state ordering, likely due to enhanced importance of through-bond electronic effects in determining the stability of metal−oxo intermediates. We then used an ML model to enumerate the space spanned by our ligand set, enabling widespread determination of spin- and metal-dependent trends. The enumeration also revealed unexpected metal/ligand-property relationships, such as reduced spin-state dependence in Fe(IV)═O complexes with strong-field equatorial ligands

DOI: 10.1021/acscatal.9b02165
ACS Catal. 2019, 9, 8243−8255

and weak-field axial ligands that instead increased spin-state dependence for Co(V)=O complexes.

In contrast with earlier computational screens where the β-HOMO level of an M(II) complex could be shown to predict its M(IV)=O stability, we observed only weak correlation over our DFT data sets. Full ANN enumeration of both properties in this space revealed opportunities to break this design rule by producing oxidatively stable complexes that favorably form oxo intermediates. We then expanded the search space to over 37 000 catalysts by introducing new ligands and used a multicomponent GA to discover candidate catalysts that defy expectations but could still be confidently predicted by our ANN models. Using this approach, we identified both favorable oxo formation energies for oxidatively stable complexes (i.e., a typical target for a catalyst screen) and unfavorable oxo formation energies for oxidatively unstable complexes (i.e., a combination unexpected by intuition). This approach doubled the number of DFT hits that satisfied these constraints, including complexes distinct from what had been seen before in DFT training data. These observations point to the opportunities for ML-model driven discovery to both identify desirable catalysts where Edisonian approaches have failed and to find ways to break rules when known exceptions are limited. Next steps beyond the current approach will be to consider multiple reaction steps, transition states, and through-space interactions neglected thus far in our representations.

■ ASSOCIATED CONTENT

Ⓢ Supporting Information

The Supporting Information is available free of charge on the ACS Publications website at DOI: 10.1021/acscatal.9b02165.

Ligands from both data sets; statistics of data sets separated by metal, oxidation state, and spin state; criteria used for geometry checks, failure modes, and counts for the equatorially symmetric set; hyperparameters and training information for KRR and ANN models; random forest preordered recursive feature addition (RF-RFA) for both data sets; distribution of oxo formation energies and comparisons to previous work on spin-splitting energies; nonfeature-selected KRR model performance; features selected on both data sets and comparisons between feature sets; comparison of M06-L/def2-TZVP vs B3LYP/LACVP* oxo formation energies sorted by connecting atom identity; structures of endothermically biased oxo formation energies by M06-L/def2-TZVP; train and test performance of KRR models for M06-L/def2-TZVP data; KRR errors decomposed by metal, oxidation state, and/or arrangement; d-orbital character of empty-site β-HOMO in quintet Fe complexes and full equatorially symmetric set; empty-site β-HOMO level vs oxo structure energetic HOMO level; comparison of previously published frontier orbital energetics data set to equatorially symmetric data set; application of previously published model for frontier orbital energetics on equatorially symmetric data; full enumeration predictions by the feature-selected KRR/ANN models; histogram of deviations between the feature-selected KRR and ANN models; ANN enumerated oxo formation energy vs β-HOMO level; placement of oxo formation energy and β-HOMO level for a 277 molecule validation set; plot of absolute errors for β-HOMO level and oxo formation energy; expanded ligand space used in the genetic algorithm (GA) exploration; latent distance cutoff calibration; evolution of the GA by generation for both zones; average distance and diversity over the 10 replicates for each targeted zone; examples for feature space vs latent space distances (PDF)

Structures from the equatorially symmetric data set; 277 molecule DFT validation data set; GA lead compounds from Zones 1 and 2; raw electronic energies for the equatorially symmetric data set (B3LYP/LACVP* and M06L/def2-TZVP), equatorially asymmetric data set, 277 molecule DFT validation data set, and GA lead compounds from Zones 1 and 2; RAC featurization for equatorially symmetric and equatorially asymmetric data sets (ZIP)

■ AUTHOR INFORMATION

Corresponding Authors

*E-mail: rgetman@g.clemson.edu. Phone: 864-656-5423.
*E-mail: hjkulik@mit.edu. Phone: 617-253-4584.

ORCID

Aditya Nandy: 0000-0001-7137-5449
Jon Paul Janet: 0000-0001-7825-4797
Chenru Duan: 0000-0003-2592-4237
Heather J. Kulik: 0000-0001-9342-0191

Notes

The authors declare no competing financial interest.

■ ACKNOWLEDGMENTS

This work was supported by the Inorganometallic Catalyst Design Center, an EFRC funded by the DOE, Office of Basic Energy Sciences (DE-SC0012702). This work used the XStream computational resource, supported by the National Science Foundation Major Research Instrumentation program (ACI-1429830). This work was carried out in part using computational resources from the Extreme Science and Engineering Discovery Environment (XSEDE), which is supported by National Science Foundation grant number ACI-1548562. Simulations were also performed on the Palmetto Supercomputer Cluster, which is maintained by the Cyberinfrastructure Technology Integration Group at Clemson University. H.J.K. holds a Career Award at the Scientific Interface from the Burroughs Wellcome Fund and an AAAS Marion Milligan Mason Award, which partly supported this work. The authors thank Adam H. Steeves for providing a critical reading of the manuscript.

■ REFERENCES

(1) Lunsford, J. H. Catalytic Conversion of Methane to More Useful Chemicals and Fuels: A Challenge for the 21st Century. *Catal. Today* **2000**, *63*, 165−174.

(2) Olah, G. A. Beyond Oil and Gas: The Methanol Economy. *Angew. Chem., Int. Ed.* **2005**, *44*, 2636−2639.

(3) Periana, R. A.; Taube, D. J.; Gamble, S.; Taube, H.; Satoh, T.; Fujii, H. Platinum Catalysts for the High-Yield Oxidation of Methane to a Methanol Derivative. *Science* **1998**, *280*, 560−564.

(4) Muehlhofer, M.; Strassner, T.; Herrmann, W. A. New Catalyst Systems for the Catalytic Conversion of Methane into Methanol. *Angew. Chem., Int. Ed.* **2002**, *41*, 1745−1747.

(5) Jones, C.; Taube, D.; Ziatdinov, V. R.; Periana, R. A.; Nielsen, R. J.; Oxgaard, J.; Goddard, W. A. Selective Oxidation of Methane to Methanol Catalyzed, with C-H Activation, by Homogeneous, Cationic Gold. *Angew. Chem.* **2004**, *116*, 4726−4729.

DOI: 10.1021/acscatal.9b02165
ACS Catal. 2019, 9, 8243−8255

(6) Palkovits, R.; Antonietti, M.; Kuhn, P.; Thomas, A.; Schüth, F. Solid Catalysts for the Selective Low-Temperature Oxidation of Methane to Methanol. *Angew. Chem., Int. Ed.* **2009**, *48*, 6909−6912.
(7) Hammond, C.; Forde, M. M.; Ab Rahim, M. H.; Thetford, A.; He, Q.; Jenkins, R. L.; Dimitratos, N.; Lopez-Sanchez, J. A.; Dummer, N. F. Direct Catalytic Conversion of Methane to Methanol in an Aqueous Medium by Using Copper-Promoted Fe-Zsm-5. *Angew. Chem., Int. Ed.* **2012**, *51*, 5129−5133.
(8) Narsimhan, K.; Iyoki, K.; Dinh, K.; Roman-Leshkov, Y. Catalytic Oxidation of Methane into Methanol over Copper-Exchanged Zeolites with Oxygen at Low Temperature. *ACS Cent. Sci.* **2016**, *2*, 424−429.
(9) Wang, V. C.-C.; Maji, S.; Chen, P. P.-Y.; Lee, H. K.; Yu, S. S.-F.; Chan, S. I. Alkane Oxidation: Methane Monooxygenases, Related Enzymes, and Their Biomimetics. *Chem. Rev.* **2017**, *117*, 8574−8621.
(10) Eichhorn, E.; van der Ploeg, J. R.; Kertesz, M. A.; Leisinger, T. Characterization of A-Ketoglutarate-Dependent Taurine Dioxygenase from Escherichia Coli. *J. Biol. Chem.* **1997**, *272*, 23031−23036.
(11) Price, J. C.; Barr, E. W.; Glass, T. E.; Krebs, C.; Bollinger, J. M. Evidence for Hydrogen Abstraction from C1 of Taurine by the High-Spin Fe (IV) Intermediate Detected During Oxygen Activation by Taurine: A-Ketoglutarate Dioxygenase (Taud). *J. Am. Chem. Soc.* **2003**, *125*, 13008−13009.
(12) Price, J. C.; Barr, E. W.; Tirupati, B.; Bollinger, J. M.; Krebs, C. The First Direct Characterization of a High-Valent Iron Intermediate in the Reaction of an A-Ketoglutarate-Dependent Dioxygenase: A High-Spin Fe (IV) Complex in Taurine/A-Ketoglutarate Dioxygenase (Taud) from Escherichia Coli. *Biochemistry* **2003**, *42*, 7497−7508.
(13) Que, L., Jr.; Tolman, W. B. Biologically Inspired Oxidation Catalysis. *Nature* **2008**, *455*, 333−40.
(14) Nam, W.; Lee, Y.-M.; Fukuzumi, S. Tuning Reactivity and Mechanism in Oxidation Reactions by Mononuclear Nonheme Iron (IV)-Oxo Complexes. *Acc. Chem. Res.* **2014**, *47*, 1146−1154.
(15) Nam, W. Synthetic Mononuclear Nonheme Iron-Oxygen Intermediates. *Acc. Chem. Res.* **2015**, *48*, 2415−2423.
(16) Engelmann, X.; Monte-Perez, I.; Ray, K. Oxidation Reactions with Bioinspired Mononuclear Non-Heme Metal-Oxo Complexes. *Angew. Chem., Int. Ed.* **2016**, *55*, 7632−49.
(17) Kim, S. O.; Sastri, C. V.; Seo, M. S.; Kim, J.; Nam, W. Dioxygen Activation and Catalytic Aerobic Oxidation by a Mononuclear Nonheme Iron(II) Complex. *J. Am. Chem. Soc.* **2005**, *127*, 4178−9.
(18) Grundner, S.; Markovits, M. A.; Li, G.; Tromp, M.; Pidko, E. A.; Hensen, E. J.; Jentys, A.; Sanchez-Sanchez, M.; Lercher, J. A. Single-Site Trinuclear Copper Oxygen Clusters in Mordenite for Selective Conversion of Methane to Methanol. *Nat. Commun.* **2015**, *6*, 7546.
(19) Snyder, B. E. R.; Böttger, L. H.; Bols, M. L.; Yan, J. J.; Rhoda, H. M.; Jacobs, A. B.; Hu, M. Y.; Zhao, J.; Alp, E. E.; Hedman, B.; Hodgson, K. O.; Schoonheydt, R. A.; Sels, B. F.; Solomon, E. I. Structural Characterization of a Non-Heme Iron Active Site in Zeolites That Hydroxylates Methane. *Proc. Natl. Acad. Sci. U. S. A.* **2018**, *115*, 4565−4570.
(20) Osadchii, D. Y.; Olivos-Suarez, A. I.; Szécsényi, Á.; Li, G.; Nasalevich, M. A.; Dugulan, I. A.; Crespo, P. S.; Hensen, E. J.; Veber, S. L.; Fedin, M. V. Isolated Fe Sites in Metal Organic Frameworks Catalyze the Direct Conversion of Methane to Methanol. *ACS Catal.* **2018**, *8*, 5542−5548.
(21) Borovik, A. S. Role of Metal-Oxo Complexes in the Cleavage of C-H Bonds. *Chem. Soc. Rev.* **2011**, *40*, 1870−4.
(22) Chantarojsiri, T.; Ziller, J. W.; Yang, J. Y. Incorporation of Redox-Inactive Cations Promotes Iron Catalyzed Aerobic C−H Oxidation at Mild Potentials. *Chem. Sci.* **2018**, *9*, 2567−2574.
(23) Grapperhaus, C. A.; Mienert, B.; Bill, E.; Weyhermüller, T.; Wieghardt, K. Mononuclear (Nitrido)Iron(V) and (Oxo)Iron(IV) Complexes via Photolysis of [(Cyclam-Acetato)Feiii(N3)]+and Ozonolysis of [(Cyclam-Acetato)Feiii(O3scf3)]+in Water/Acetone Mixtures‡. *Inorg. Chem.* **2000**, *39*, 5306−5317.
(24) de Oliveira, F. T.; Chanda, A.; Banerjee, D.; Shan, X.; Mondal, S.; Que, L.; Bominaar, E. L.; Munck, E.; Collins, T. J. Chemical and Spectroscopic Evidence for an FeV-oxo Complex. *Science* **2007**, *315*, 835−838.
(25) Chen, K.; Que, L. Stereospecific Alkane Hydroxylation by Non-Heme Iron Catalysts: Mechanistic Evidence for an FeVO Active Species. *J. Am. Chem. Soc.* **2001**, *123*, 6327−6337.
(26) Parsell, T. H.; Behan, R. K.; Green, M. T.; Hendrich, M. P.; Borovik, A. S. Preparation and Properties of a Monomeric Mn(IV)-Oxo Complex. *J. Am. Chem. Soc.* **2006**, *128*, 8728−9.
(27) Gupta, R.; Taguchi, T.; Lassalle-Kaiser, B.; Bominaar, E. L.; Yano, J.; Hendrich, M. P.; Borovik, A. S. High-Spin Mn-Oxo Complexes and Their Relevance to the Oxygen-Evolving Complex within Photosystem II. *Proc. Natl. Acad. Sci. U. S. A.* **2015**, *112*, 5319−24.
(28) Neu, H. M.; Yang, T.; Baglia, R. A.; Yosca, T. H.; Green, M. T.; Quesne, M. G.; de Visser, S. P.; Goldberg, D. P. Oxygen-Atom Transfer Reactivity of Axially Ligated Mn(V)-Oxo Complexes: Evidence for Enhanced Electrophilic and Nucleophilic Pathways. *J. Am. Chem. Soc.* **2014**, *136*, 13845−52.
(29) Pestovsky, O.; Stoian, S.; Bominaar, E. L.; Shan, X.; Munck, E.; Que, L., Jr.; Bakac, A. Aqueous Feiv = =O: Spectroscopic Identification and Oxo-Group Exchange. *Angew. Chem., Int. Ed.* **2005**, *44*, 6871−4.
(30) Rohde, J. U.; Torelli, S.; Shan, X.; Lim, M. H.; Klinker, E. J.; Kaizer, J.; Chen, K.; Nam, W.; Que, L., Jr. Structural Insights into Nonheme Alkylperoxoiron(III) and Oxoiron(IV) Intermediates by X-Ray Absorption Spectroscopy. *J. Am. Chem. Soc.* **2004**, *126*, 16750−61.
(31) McDonald, A. R.; Que, L. High-Valent Nonheme Iron-Oxo Complexes: Synthesis, Structure, and Spectroscopy. *Coord. Chem. Rev.* **2013**, *257*, 414−428.
(32) Gupta, R.; Lacy, D. C.; Bominaar, E. L.; Borovik, A. S.; Hendrich, M. P. Electron Paramagnetic Resonance and Mossbauer Spectroscopy and Density Functional Theory Analysis of a High-Spin Fe(IV)-Oxo Complex. *J. Am. Chem. Soc.* **2012**, *134*, 9775−84.
(33) Vogiatzis, K. D.; Haldoupis, E.; Xiao, D. J.; Long, J. R.; Siepmann, J. I.; Gagliardi, L. Accelerated Computational Analysis of Metal−Organic Frameworks for Oxidation Catalysis. *J. Phys. Chem. C* **2016**, *120*, 18707−18712.
(34) Betley, T. A.; Wu, Q.; Van Voorhis, T.; Nocera, D. G. Electronic Design Criteria for O-O Bond Formation via Metal-Oxo Complexes. *Inorg. Chem.* **2008**, *47*, 1849−61.
(35) Klein, J. E.; Knizia, G. Cpcet Versus Hat: A Direct Theoretical Method for Distinguishing X−H Bond-Activation Mechanisms. *Angew. Chem.* **2018**, *130*, 12089−12093.
(36) Geng, C.; Ye, S.; Neese, F. Analysis of Reaction Channels for Alkane Hydroxylation by Nonheme Iron(IV)-Oxo Complexes. *Angew. Chem., Int. Ed.* **2010**, *49*, 5717−20.
(37) Venturinelli Jannuzzi, S. A.; Phung, Q. M.; Domingo, A.; Formiga, A. L.; Pierloot, K. Spin State Energetics and Oxyl Character of Mn-Oxo Porphyrins by Multiconfigurational Ab Initio Calculations: Implications on Reactivity. *Inorg. Chem.* **2016**, *55*, 5168−79.
(38) Lai, W.; Cao, R.; Dong, G.; Shaik, S.; Yao, J.; Chen, H. Why Is Cobalt the Best Transition Metal in Transition-Metal Hangman Corroles for O-O Bond Formation During Water Oxidation? *J. Phys. Chem. Lett.* **2012**, *3*, 2315−9.
(39) Pellizzeri, S.; Barona, M.; Bernales, V.; Miró, P.; Liao, P.; Gagliardi, L.; Snurr, R. Q.; Getman, R. B. Catalytic Descriptors and Electronic Properties of Single-Site Catalysts for Ethene Dimerization to 1-Butene. *Catal. Today* **2018**, *312*, 149−157.
(40) Andris, E.; Navratil, R.; Jasik, J.; Puri, M.; Costas, M.; Que, L., Jr.; Roithova, J. Trapping Iron(III)-Oxo Species at the Boundary of the ″Oxo Wall″: Insights into the Nature of the Fe(III)-O Bond. *J. Am. Chem. Soc.* **2018**, *140*, 14391−14400.
(41) Gray, H. B.; Winkler, J. R. Living with Oxygen. *Acc. Chem. Res.* **2018**, *51*, 1850−1857.
(42) O'Halloran, K. P.; Zhao, C.; Ando, N. S.; Schultz, A. J.; Koetzle, T. F.; Piccoli, P. M. B.; Hedman, B.; Hodgson, K. O.; Bobyr, E.; Kirk, M. L.; Knottenbelt, S.; Depperman, E. C.; Stein, B.; Anderson, T. M.; Cao, R.; Geletii, Y. V.; Hardcastle, K. I.; Musaev, D. G.; Neiwert, W.

A.; Fang, X.; Morokuma, K.; Wu, S.; Kögerler, P.; Hill, C. L. Revisiting the Polyoxometalate-Based Late-Transition-Metal-Oxo Complexes: The "Oxo Wall" Stands. *Inorg. Chem.* **2012**, *51*, 7025–7031.

(43) Holm, R. H. Metal-Centered Oxygen Atom Transfer Reactions. *Chem. Rev.* **1987**, *87*, 1401–1449.

(44) Saracini, C.; Malik, D. D.; Sankaralingam, M.; Lee, Y. M.; Nam, W.; Fukuzumi, S. Enhanced Electron-Transfer Reactivity of a Long-Lived Photoexcited State of a Cobalt-Oxygen Complex. *Inorg. Chem.* **2018**, *57*, 10945–10952.

(45) Das, D.; Pattanayak, S.; Singh, K. K.; Garai, B.; Sen Gupta, S. Electrocatalytic Water Oxidation by a Molecular Cobalt Complex through a High Valent Cobalt Oxo Intermediate. *Chem. Commun. (Cambridge, U. K.)* **2016**, *52*, 11787–11790.

(46) Andris, E.; Navratil, R.; Jasik, J.; Srnec, M.; Rodriguez, M.; Costas, M.; Roithová, J. M–O Bonding Beyond the Oxo Wall: Spectroscopy and Reactivity of Cobalt(III)-Oxyl and Cobalt(III)-Oxo Complexes. *Angew. Chem., Int. Ed.* **2019**, *58*, 9619–9624.

(47) Decker, A.; Rohde, J. U.; Klinker, E. J.; Wong, S. D.; Que, L., Jr.; Solomon, E. I. Spectroscopic and Quantum Chemical Studies on Low-Spin FeIV═O Complexes: Fe-O Bonding and Its Contributions to Reactivity. *J. Am. Chem. Soc.* **2007**, *129*, 15983–15996.

(48) Betley, T. A.; Surendranath, Y.; Childress, M. V.; Alliger, G. E.; Fu, R.; Cummins, C. C.; Nocera, D. G. A Ligand Field Chemistry of Oxygen Generation by the Oxygen-Evolving Complex and Synthetic Active Sites. *Philos. Trans. R. Soc., B* **2008**, *363*, 1293–303.

(49) Bernasconi, L.; Louwerse, M. J.; Baerends, E. J. The Role of Equatorial and Axial Ligands in Promoting the Activity of Non-Heme Oxidoiron(IV) Catalysts in Alkane Hydroxylation. *Eur. J. Inorg. Chem.* **2007**, *2007*, 3023–3033.

(50) Hirao, H.; Kumar, D.; Que, L., Jr.; Shaik, S. Two-State Reactivity in Alkane Hydroxylation by Non-Heme Iron-Oxo Complexes. *J. Am. Chem. Soc.* **2006**, *128*, 8590–606.

(51) Shaik, S.; Hirao, H.; Kumar, D. Reactivity of High-Valent Iron-Oxo Species in Enzymes and Synthetic Reagents: A Tale of Many States. *Acc. Chem. Res.* **2007**, *40*, 532–42.

(52) Kupper, C.; Mondal, B.; Serrano-Plana, J.; Klawitter, I.; Neese, F.; Costas, M.; Ye, S.; Meyer, F. Nonclassical Single-State Reactivity of an Oxo-Iron(IV) Complex Confined to Triplet Pathways. *J. Am. Chem. Soc.* **2017**, *139*, 8939–8949.

(53) Janardanan, D.; Wang, Y.; Schyman, P.; Que, L., Jr.; Shaik, S. The Fundamental Role of Exchange-Enhanced Reactivity in C-H Activation by S = 2 Oxo Iron(IV) Complexes. *Angew. Chem., Int. Ed.* **2010**, *49*, 3342–5.

(54) Company, A.; Prat, I.; Frisch, J. R.; Mas-Balleste, D. R.; Guell, M.; Juhasz, G.; Ribas, X.; Munck, D. E.; Luis, J. M.; Que, L.; Costas, M. Modeling the Cis-Oxo-Labile Binding Site Motif of Non-Heme Iron Oxygenases: Water Exchange and Oxidation Reactivity of a Non-Heme Iron(IV)-Oxo Compound Bearing a Tripodal Tetradentate Ligand. *Chem. - Eur. J.* **2011**, *17*, 1622–1634.

(55) Klinker, E. J.; Kaizer, J.; Brennessel, W. W.; Woodrum, N. L.; Cramer, C. J.; Que, L., Jr. Structures of Nonheme Oxoiron(IV) Complexes from X-Ray Crystallography, NMR Spectroscopy, and DFT Calculations. *Angew. Chem., Int. Ed.* **2005**, *44*, 3690–4.

(56) Lim, M. H.; Rohde, J. U.; Stubna, A.; Bukowski, M. R.; Costas, M.; Ho, R. Y.; Munck, E.; Nam, W.; Que, L., Jr. An FeIV═O Complex of a Tetradentate Tripodal Nonheme Ligand. *Proc. Natl. Acad. Sci. U. S. A.* **2003**, *100*, 3665–70.

(57) Kaizer, J.; Klinker, E. J.; Oh, N. Y.; Rohde, J. U.; Song, W. J.; Stubna, A.; Kim, J.; Munck, E.; Nam, W.; Que, L., Jr. Nonheme Feivo Complexes That Can Oxidize the C-H Bonds of Cyclohexane at Room Temperature. *J. Am. Chem. Soc.* **2004**, *126*, 472–3.

(58) Rosen, A. S.; Notestein, J. M.; Snurr, R. Q. Structure–Activity Relationships That Identify Metal–Organic Framework Catalysts for Methane Activation. *ACS Catal.* **2019**, *9*, 3576–3587.

(59) Ortuño, M. A.; Bernales, V.; Gagliardi, L.; Cramer, C. J. Computational Study of First-Row Transition Metals Supported on Mof Nu-1000 for Catalytic Acceptorless Alcohol Dehydrogenation. *J. Phys. Chem. C* **2016**, *120*, 24697–24705.

(60) Pahls, D. R.; Ortuño, M. A.; Winegar, P. H.; Cramer, C. J.; Gagliardi, L. Computational Screening of Bimetal-Functionalized Zr6o8Mof Nodes for Methane C-H Bond Activation. *Inorg. Chem.* **2017**, *56*, 8739–8743.

(61) Andrikopoulos, P. C.; Michel, C.; Chouzier, S.; Sautet, P. In Silico Screening of Iron-Oxo Catalysts for CH Bond Cleavage. *ACS Catal.* **2015**, *5*, 2490–2499.

(62) Schenk, S.; Reiher, M. Ligands for Dinitrogen Fixation at Schrock-Type Catalysts. *Inorg. Chem.* **2009**, *48*, 1638–1648.

(63) Greeley, J.; Jaramillo, T. F.; Bonde, J.; Chorkendorff, I.; Nørskov, J. K. Computational High-Throughput Screening of Electrocatalytic Materials for Hydrogen Evolution. *Nat. Mater.* **2006**, *5*, 909–913.

(64) Andersson, M. P.; Bligaard, T.; Kustov, A.; Larsen, K. E.; Greeley, J.; Johannessen, T.; Christensen, C. H.; Nørskov, J. K. Toward Computational Screening in Heterogeneous Catalysis: Pareto-Optimal Methanation Catalysts. *J. Catal.* **2006**, *239*, 501–506.

(65) Nørskov, J. K.; Bligaard, T.; Rossmeisl, J.; Christensen, C. H. Towards the Computational Design of Solid Catalysts. *Nat. Chem.* **2009**, *1*, 37–46.

(66) Kim, J. Y.; Kulik, H. J. When Is Ligand pKa a Good Descriptor for Catalyst Energetics? In Search of Optimal CO2 Hydration Catalysts. *J. Phys. Chem. A* **2018**, *122*, 4579–4590.

(67) Gani, T. Z. H.; Kulik, H. J. Understanding and Breaking Scaling Relations in Single-Site Catalysis: Methane-to-Methanol Conversion by Fe(IV)═O. *ACS Catal.* **2018**, *8*, 975–986.

(68) Latimer, A. A.; Kulkarni, A. R.; Aljama, H.; Montoya, J. H.; Yoo, J. S.; Tsai, C.; Abild-Pedersen, F.; Studt, F.; Nørskov, J. K. Understanding Trends in C–H Bond Activation in Heterogeneous Catalysis. *Nat. Mater.* **2017**, *16*, 225.

(69) Vogiatzis, K. D.; Polynski, M. V.; Kirkland, J. K.; Townsend, J.; Hashemi, A.; Liu, C.; Pidko, E. A. Computational Approach to Molecular Catalysis by 3d Transition Metals: Challenges and Opportunities. *Chem. Rev.* **2019**, *119*, 2453–2523.

(70) Liao, P.; Getman, R. B.; Snurr, R. Q. Optimizing Open Iron Sites in Metal–Organic Frameworks for Ethane Oxidation: A First-Principles Study. *ACS Appl. Mater. Interfaces* **2017**, *9*, 33484–33492.

(71) Abild-Pedersen, F.; Greeley, J.; Studt, F.; Rossmeisl, J.; Munter, T.; Moses, P. G.; Skulason, E.; Bligaard, T.; Nørskov, J. K. Scaling Properties of Adsorption Energies for Hydrogen-Containing Molecules on Transition-Metal Surfaces. *Phys. Rev. Lett.* **2007**, *99*, 016105.

(72) Montemore, M. M.; Medlin, J. W. Scaling Relations between Adsorption Energies for Computational Screening and Design of Catalysts. *Catal. Sci. Technol.* **2014**, *4*, 3748–3761.

(73) Greeley, J. Theoretical Heterogeneous Catalysis: Scaling Relationships and Computational Catalyst Design. *Annu. Rev. Chem. Biomol. Eng.* **2016**, *7*, 605–635.

(74) Bligaard, T.; Nørskov, J. K.; Dahl, S.; Matthiesen, J.; Christensen, C. H.; Sehested, J. The Brønsted–Evans–Polanyi Relation and the Volcano Curve in Heterogeneous Catalysis. *J. Catal.* **2004**, *224*, 206–217.

(75) van Santen, R. A.; Neurock, M.; Shetty, S. G. Reactivity Theory of Transition-Metal Surfaces: A Brønsted- Evans- Polanyi Linear Activation Energy- Free-Energy Analysis. *Chem. Rev.* **2010**, *110*, 2005–2048.

(76) Man, I. C.; Su, H. Y.; Calle-Vallejo, F.; Hansen, H. A.; Martínez, J. I.; Inoglu, N. G.; Kitchin, J.; Jaramillo, T. F.; Nørskov, J. K.; Rossmeisl, J. Universality in Oxygen Evolution Electrocatalysis on Oxide Surfaces. *ChemCatChem* **2011**, *3*, 1159–1165.

(77) Peterson, A. A.; Nørskov, J. K. Activity Descriptors for CO2 Electroreduction to Methane on Transition-Metal Catalysts. *J. Phys. Chem. Lett.* **2012**, *3*, 251–258.

(78) Hammer, B.; Nørskov, J. Electronic Factors Determining the Reactivity of Metal Surfaces. *Surf. Sci.* **1995**, *343*, 211–220.

(79) Hammer, B.; Nørskov, J. K. Why Gold Is the Noblest of All the Metals. *Nature* **1995**, *376*, 238–240.

(80) Hammer, B.; Nørskov, J. K. Theoretical Surface Science and Catalysis—Calculations and Concepts. *Adv. Catal.* **2000**, *45*, 71–129.

DOI: 10.1021/acscatal.9b02165
ACS Catal. 2019, 9, 8243–8255

(81) Ketrat, S.; Maihom, T.; Wannakao, S.; Probst, M.; Nokbin, S.; Limtrakul, J. Coordinatively Unsaturated Metal-Organic Frameworks M3(Btc)2 (M = Cr, Fe, Co, Ni, Cu, and Zn) Catalyzing the Oxidation of CO by N2o: Insight from DFT Calculations. *Inorg. Chem.* **2017**, *56*, 14005−14012.

(82) Shaik, S.; Chen, H.; Janardanan, D. Exchange-Enhanced Reactivity in Bond Activation by Metal-Oxo Enzymes and Synthetic Reagents. *Nat. Chem.* **2011**, *3*, 19−27.

(83) Calle-Vallejo, F.; Martínez, J. I.; Rossmeisl, J. Density Functional Studies of Functionalized Graphitic Materials with Late Transition Metals for Oxygen Reduction Reactions. *Phys. Chem. Chem. Phys.* **2011**, *13*, 15639−15643.

(84) Gani, T. Z. H.; Ioannidis, E. I.; Kulik, H. J. Computational Discovery of Hydrogen Bond Design Rules for Electrochemical Ion Separation. *Chem. Mater.* **2016**, *28*, 6207−6218.

(85) Lacy, D. C.; Gupta, R.; Stone, K. L.; Greaves, J.; Ziller, J. W.; Hendrich, M. P.; Borovik, A. S. Formation, Structure, and Epr Detection of a High Spin Fe(IV)-Oxo Species Derived from Either an Fe(III)-Oxo or Fe(III)-Oh Complex. *J. Am. Chem. Soc.* **2010**, *132*, 12188−90.

(86) Shook, R. L.; Borovik, A. S. Role of the Secondary Coordination Sphere in Metal-Mediated Dioxygen Activation. *Inorg. Chem.* **2010**, *49*, 3646−3660.

(87) Cook, S. A.; Borovik, A. S. Molecular Designs for Controlling the Local Environments around Metal Ions. *Acc. Chem. Res.* **2015**, *48*, 2407−2414.

(88) Goldsmith, B. R.; Esterhuizen, J.; Liu, J. X.; Bartel, C. J.; Sutton, C. Machine Learning for Heterogeneous Catalyst Design and Discovery. *AIChE J.* **2018**, *64*, 2311−2323.

(89) Kitchin, J. R. Machine Learning in Catalysis. *Nat. Catal.* **2018**, *1*, 230.

(90) Butler, K. T.; Davies, D. W.; Cartwright, H.; Isayev, O.; Walsh, A. Machine Learning for Molecular and Materials Science. *Nature* **2018**, *559*, 547.

(91) Ramprasad, R.; Batra, R.; Pilania, G.; Mannodi-Kanakkithodi, A.; Kim, C. Machine Learning in Materials Informatics: Recent Applications and Prospects. *npj Comput. Mater.* **2017**, *3*, 54.

(92) Janet, J. P.; Liu, F.; Nandy, A.; Duan, C.; Yang, T.; Lin, S.; Kulik, H. J. Designing in the Face of Uncertainty: Exploiting Electronic Structure and Machine Learning Models for Discovery in Inorganic Chemistry. *Inorg. Chem.* **2019**, DOI: 10.1021/acs.inorgchem.9b00109.

(93) Simm, G. N.; Reiher, M. Error-Controlled Exploration of Chemical Reaction Networks with Gaussian Processes. *J. Chem. Theory Comput.* **2018**, *14*, 5238−5248.

(94) Ulissi, Z. W.; Medford, A. J.; Bligaard, T.; Nørskov, J. K. To Address Surface Reaction Network Complexity Using Scaling Relations Machine Learning and DFT Calculations. *Nat. Commun.* **2017**, *8*, 14621.

(95) Ma, X.; Li, Z.; Achenie, L. E. K.; Xin, H. Machine-Learning-Augmented Chemisorption Model for CO2 Electroreduction Catalyst Screening. *J. Phys. Chem. Lett.* **2015**, *6*, 3528−3533.

(96) Meyer, B.; Sawatlon, B.; Heinen, S.; von Lilienfeld, O. A.; Corminboeuf, C. Machine Learning Meets Volcano Plots: Computational Discovery of Cross-Coupling Catalysts. *Chem. Sci.* **2018**, *9*, 7069−7077.

(97) Tran, K.; Ulissi, Z. W. Active Learning across Intermetallics to Guide Discovery of Electrocatalysts for CO2 Reduction and H2 Evolution. *Nat. Catal.* **2018**, *1*, 696.

(98) Nandy, A.; Duan, C.; Janet, J. P.; Gugler, S.; Kulik, H. J. Strategies and Software for Machine Learning Accelerated Discovery in Transition Metal Chemistry. *Ind. Eng. Chem. Res.* **2018**, *57*, 13973−13986.

(99) Li, Z.; Omidvar, N.; Chin, W. S.; Robb, E.; Morris, A.; Achenie, L.; Xin, H. Machine-Learning Energy Gaps of Porphyrins with Molecular Graph Representations. *J. Phys. Chem. A* **2018**, *122*, 4571−4578.

(100) Janet, J. P.; Gani, T. Z. H.; Steeves, A. H.; Ioannidis, E. I.; Kulik, H. J. Leveraging Cheminformatics Strategies for Inorganic Discovery: Application to Redox Potential Design. *Ind. Eng. Chem. Res.* **2017**, *56*, 4898−4910.

(101) Janet, J. P.; Kulik, H. J. Resolving Transition Metal Chemical Space: Feature Selection for Machine Learning and Structure−Property Relationships. *J. Phys. Chem. A* **2017**, *121*, 8939−8954.

(102) Janet, J. P.; Chan, L.; Kulik, H. J. Accelerating Chemical Discovery with Machine Learning: Simulated Evolution of Spin Crossover Complexes with an Artificial Neural Network. *J. Phys. Chem. Lett.* **2018**, *9*, 1064−1071.

(103) Janet, J. P.; Kulik, H. J. Predicting Electronic Structure Properties of Transition Metal Complexes with Neural Networks. *Chem. Sci.* **2017**, *8*, 5137−5152.

(104) Janet, J. P.; Duan, C.; Yang, T.; Nandy, A.; Kulik, H. A Quantitative Uncertainty Metric Controls Error in Neural Network-Driven Chemical Discovery. *Chem. Sci.* **2019**, DOI: 10.1039/C9SC02298H.

(105) Zandkarimi, B.; Alexandrova, A. N. Dynamics of Subnanometer Pt Clusters Can Break the Scaling Relationships in Catalysis. *J. Phys. Chem. Lett.* **2019**, *10*, 460−467.

(106) Darby, M. T.; Stamatakis, M.; Michaelides, A.; Sykes, E. C. H. Lonely Atoms with Special Gifts: Breaking Linear Scaling Relationships in Heterogeneous Catalysis with Single-Atom Alloys. *J. Phys. Chem. Lett.* **2018**, *9*, 5636−5646.

(107) Ufimtsev, I. S.; Martinez, T. J. Quantum Chemistry on Graphical Processing Units. 3. Analytical Energy Gradients, Geometry Optimization, and First Principles Molecular Dynamics. *J. Chem. Theory Comput.* **2009**, *5*, 2619−2628.

(108) Petachem. Terachem; http://www.petachem.com (accessed May 17, 2019).

(109) Lee, C.; Yang, W.; Parr, R. G. Development of the Colle-Salvetti Correlation-Energy Formula into a Functional of the Electron Density. *Phys. Rev. B: Condens. Matter Mater. Phys.* **1988**, *37*, 785−789.

(110) Becke, A. D. Density-Functional Thermochemistry. III. The Role of Exact Exchange. *J. Chem. Phys.* **1993**, *98*, 5648−5652.

(111) Stephens, P. J.; Devlin, F. J.; Chabalowski, C. F.; Frisch, M. J. Ab Initio Calculation of Vibrational Absorption and Circular Dichroism Spectra Using Density Functional Force Fields. *J. Phys. Chem.* **1994**, *98*, 11623−11627.

(112) Grimme, S.; Antony, J.; Ehrlich, S.; Krieg, H. A Consistent and Accurate Ab Initio Parametrization of Density Functional Dispersion Correction (DFT-D) for the 94 Elements H-Pu. *J. Chem. Phys.* **2010**, *132*, 154104.

(113) Becke, A. D.; Johnson, E. R. A Density-Functional Model of the Dispersion Interaction. *J. Chem. Phys.* **2005**, *123*, 154101.

(114) Johnson, E. R.; Becke, A. D. A Post-Hartree−Fock Model of Intermolecular Interactions. *J. Chem. Phys.* **2005**, *123*, 024101.

(115) Johnson, E. R.; Becke, A. D. A Post-Hartree-Fock Model of Intermolecular Interactions: Inclusion of Higher-Order Corrections. *J. Chem. Phys.* **2006**, *124*, 174104.

(116) Hay, P. J.; Wadt, W. R. Ab Initio Effective Core Potentials for Molecular Calculations. Potentials for the Transition Metal Atoms Sc to Hg. *J. Chem. Phys.* **1985**, *82*, 270−283.

(117) Ioannidis, E. I.; Gani, T. Z. H.; Kulik, H. J. molSimplify: A Toolkit for Automating Discovery in Inorganic Chemistry. *J. Comput. Chem.* **2016**, *37*, 2106−2117.

(118) Verma, P.; Vogiatzis, K. D.; Planas, N.; Borycz, J.; Xiao, D. J.; Long, J. R.; Gagliardi, L.; Truhlar, D. G. Mechanism of Oxidation of Ethane to Ethanol at Iron(IV)−Oxo Sites in Magnesium-Diluted Fe2(Dobdc). *J. Am. Chem. Soc.* **2015**, *137*, 5770−5781.

(119) Frisch, M. J.; Trucks, G. W.; Schlegel, H. B.; Scuseria, G. E.; Robb, M. A.; Cheeseman, J. R.; Scalmani, G.; Barone, V.; Mennucci, B.; Petersson, G. A.; Nakatsuji, H.; Caricato, M.; Li, X.; Hratchian, H. P.; Izmaylov, A. F.; Bloino, J.; Zheng, G.; Sonnenberg, J. L.; Hada, M.; Ehara, M.; Toyota, K.; Fukuda, R.; Hasegawa, J.; Ishida, M.; Nakajima, T.; Honda, Y.; Kitao, O.; Nakai, H.; Vreven, T.; Montgomery, J. A.; Peralta, J. E.; Ogliaro, F.; Bearpark, M.; Heyd, J. J.; Brothers, E.; Kudin, K. N.; Staroverov, V. N.; Kobayashi, R.; Normand, J.; Raghavachari, K.; Rendell, A.; Burant, J. C.; Iyengar, S.

S.; Tomasi, J.; Cossi, M.; Rega, N.; Millam, J. M.; Klene, M.; Knox, J. E.; Cross, J. B.; Bakken, V.; Adamo, C.; Jaramillo, J.; Gomperts, R.; Stratmann, R. E.; Yazyev, O.; Austin, A. J.; Cammi, R.; Pomelli, C.; Ochterski, J. W.; Martin, R. L.; Morokuma, K.; Zakrzewski, V. G.; Voth, G. A.; Salvador, P.; Dannenberg, J. J.; Dapprich, S.; Daniels, A. D.; Farkas, Foresman, J. B.; Ortiz, J. V.; Cioslowski, J.; Fox, D. J. *Gaussian 09*, Revision B.01; Gaussian, Inc.: Wallingford, CT, 2009.

(120) Zhao, Y.; Truhlar, D. G. The M06 Suite of Density Functionals for Main Group Thermochemistry, Thermochemical Kinetics, Noncovalent Interactions, Excited States, and Transition Elements: Two New Functionals and Systematic Testing of Four M06-Class Functionals and 12 Other Functionals. *Theor. Chem. Acc.* **2008**, *120*, 215−241.

(121) Weigend, F. Accurate Coulomb-Fitting Basis Sets for H to Rn. *Phys. Chem. Chem. Phys.* **2006**, *8*, 1057−65.

(122) Broto, P.; Moreau, G.; Vandycke, C. Molecular Structures: Perception, Autocorrelation Descriptor and Sar Studies: System of Atomic Contributions for the Calculation of the N-Octanol/Water Partition Coefficients. *Eur. J. Med. Chem.* **1984**, *19*, 71−78.

(123) Pedregosa, F.; Varoquaux, G.; Gramfort, A.; Michel, V.; Thirion, B.; Grisel, O.; Blondel, M.; Prettenhofer, P.; Weiss, R.; Dubourg, V. Scikit-Learn: Machine Learning in Python. *J. Mach. Learn. Res.* **2011**, *12*, 2825−2830.

(124) Keras; https://github.com/keras-team/keras (accessed May 17, 2019).

(125) Abadi, M. Tensorflow: A System for Large-Scale Machine Learning; http://www.tensorflow.org (accessed May 17, 2019).

(126) Bergstra, J.; Yamins, D.; Cox, D. D. Hyperopt: A Python Library for Optimizing the Hyperparameters of Machine Learning Algorithms. *Proceedings of the 12th Python in Science Conference*; SciPy, 2013; pp 13−20

(127) Kingma, D. P.; Ba, J. L. Adam: A Method for Stochastic Optimization. *International Conference for Learning Representations*, San Diego, CA, 2015.

(128) Chantarojsiri, T.; Sun, Y.; Long, J. R.; Chang, C. J. Water-Soluble Iron(IV)-Oxo Complexes Supported by Pentapyridine Ligands: Axial Ligand Effects on Hydrogen Atom and Oxygen Atom Transfer Reactivity. *Inorg. Chem.* **2015**, *54*, 5879−87.

(129) Kim, M. C.; Sim, E.; Burke, K. Communication: Avoiding Unbound Anions in Density Functional Calculations. *J. Chem. Phys.* **2011**, *134*, 171103.

(130) Jensen, F. Describing Anions by Density Functional Theory: Fractional Electron Affinity. *J. Chem. Theory Comput.* **2010**, *6*, 2726−35.

(131) Gunay, A.; Theopold, K. H. C-H Bond Activations by Metal Oxo Compounds. *Chem. Rev.* **2010**, *110*, 1060−81.

(132) Ballhausen, C. J.; Gray, H. B. The Electronic Structure of the Vanadyl Ion. *Inorg. Chem.* **1962**, *1*, 111−122.

(133) Winkler, J. R.; Gray, H. B. Electronic Structures of Oxo-Metal Ions. In *Molecular Electronic Structures of Transition Metal Complexes I. Structure and Bonding*, Mingos, D., Day, P., Dahl, J., Eds.; Springer, Berlin: Heidelberg, 2011; Vol. *142*, pp 17−28.

(134) Wang, B.; Lee, Y. M.; Tcho, W. Y.; Tussupbayev, S.; Kim, S. T.; Kim, Y.; Seo, M. S.; Cho, K. B.; Dede, Y.; Keegan, B. C.; Ogura, T.; Kim, S. H.; Ohta, T.; Baik, M. H.; Ray, K.; Shearer, J.; Nam, W. Synthesis and Reactivity of a Mononuclear Non-Haem Cobalt(IV)-Oxo Complex. *Nat. Commun.* **2017**, *8*, 14839.

(135) Duan, C.; Janet, J. P.; Liu, F.; Nandy, A.; Kulik, H. J. Learning from Failure: Predicting Electronic Structure Calculation Outcomes with Machine Learning Models. *J. Chem. Theory Comput.* **2019**, *15*, 2331−2345.

DOI: 10.1021/acscatal.9b02165
ACS Catal. 2019, 9, 8243−8255